Genovés, V.; Carrión García, A.; Escobar, D.; Gosálbez Castillo, J.; Monzó Balbuena, JM.; Borrachero Rosado, MV.; Paya Bernabeu, JJ. (2019). Nonlinear Acoustic Spectroscopy and Frequency Sweep Ultrasonics: Case on Thermal Damage Assessment in Mortar. Journal of Nondestructive Evaluation. 38(3):1-14. https://doi.org/10.1007/s10921-019-0599-0

**Abstract** An exhaustive study on thermal damage of Portland cement-based materials is addressed. Damage carried out at different temperatures on concrete between 40 °C and 525 °C were assessed by means of microstructural, physical and nondestructive tests. Microstructural analysis (thermogravimetry and scanning electron microscopy) showed the principal changes of the Portland cement hydrated products for the different analysed temperatures. Compressive and flexural strengths remained constant or even increased at a low heating temperature range, while the mass loss increases. Dilatometry analysis revealed important information about deformation incompatibilities between the paste and the aggregate. These results have been correlated with nondestructive tests: nonlinear impact resonance acoustic spectroscopy (NIRAS) and ultrasonic measures. The dynamic modulus and ultrasonic pulse velocity have closely predicted the linear stiffness decay of the specimens. However, hysteretic parameter from NIRAS analysis exhibited a different trend from stiffness-related parameters, keeping constant until 250 °C and suffering a huge increasing for 400 and 525 °C. Ultrasonic attenuation computed with a broadband ultrasonic signal (chirp) revealed interesting information about scattering components inside the material, and is sensitive to interfacial transition zone between aggregate and paste in a large range of frequencies. The correlation between microstructural, mechanical and nondestructive techniques were carried out successfully. Nonlinear vibration and ultrasonic attenuation are non-conventional parameters that gave specific information about a complex damage process, such as a thermal attack in highly heterogeneous materials (e.g. Portland cement composites).

# Nonlinear acoustic spectroscopy and frequency sweep ultrasonics: Case on thermal damage assessment in mortar

**Vicente Genovés · Alicia Carrión · Daniel Escobar · Jorge Gosálbez · Jose Monzó · Maria Victoria Borrachero · Jordi Payá**

the date of receipt and acceptance should be inserted later

## 1 Introduction

Thanks to its good performance against high temperatures, concrete is the most commonly used material in fire-resistant structures in civil and building engineering. Because of its great thermal inertia and insulating properties, concrete protects steel bars from fire avoiding the excessive decrease of its elastic constants [1]. Despite the usefulness of concrete, the cement paste that assembles the sand particles and coarse aggregates gradually losses stiffness and adhesion capacity when the temperature is significantly high. Several studies have evaluated the mechanical properties and general behaviour of concrete under high temperatures, mainly assessing compressive and flexural strengths, modulus of elasticity, stress-strain relationship and physical and chemical changes [2]. Several factors influence the aforementioned parameters of concrete affected by high temperatures. Water evaporation is the first mechanism of change, where the cementing matrix almost completely loses free water from the capillary network and physically absorbed water from surface of cementing C-S-H gel. At higher temperatures (105 °C), concrete starts to lose the chemically bonded water from hydrated compounds. Most of the chemically combined capillary water is lost at 400 °C. Hydration products play an important role in cement paste degradation. From 105 °C to 300 °C, a continuous mass loss due to the ettringite, C-S-H and C-A-H decomposition occurs, this brings a stiffness decay of the material but

V. Genovés
ICITECH, Universitat Politècnica de València, Camino de Vera, s/n 46022 Valencia, Spain.
E-mail: vigegme@upv.es

A. Carrión
ITEAM, Universitat Politècnica de València, Camino de Vera, s/n 46022 Valencia, Spain.
E-mail: alcarga4@upv.es

D. Escobar
ICITECH, Universitat Politècnica de València, Camino de Vera, s/n 46022 Valencia, Spain.
E-mail: fdeg_escobar@yahoo.com

J. Gosálbez
ITEAM, Universitat Politècnica de València, Camino de Vera, s/n 46022 Valencia, Spain.
E-mail: jorgocas@dcom.upv.es

J. Monzó
ICITECH, Universitat Politècnica de València, Camino de Vera, s/n 46022 Valencia, Spain.
E-mail: jmmonzo@cst.upv.es

M.V. Borrachero
ICITECH, Universitat Politècnica de València, Camino de Vera, s/n 46022 Valencia, Spain.
E-mail: vborrachero@cst.upv.es

J. Payá
ICITECH, Universitat Politècnica de València, Camino de Vera, s/n 46022 Valencia, Spain.
E-mail: jjpaya@cst.upv.es

keeps the compressive strength almost intact. From 400 °C to 525 °C, decomposition of Portlandite occurs (yielding lime, CaO), this decreases the stiffness and directly affects the compressive strength of the cement paste. However, if cement paste is water cooled after exposure to high temperature, the rehydration of lime will cause a great reduction of strength due to a considerable expansion owing to such hydration reaction [3,2].

Nevertheless, not only the loss of water plays an important role in thermal damage in concrete. According to some studies, the incompatibility of deformations between the cement paste and the aggregates is essential to understand the decay of the performance of elements made by concrete at high temperatures [4]. Limestone and quartz aggregates expand linearly until 573 °C. Quartz then experiences a great expansion due to the transformation from $\alpha$-quartz to $\beta$-quartz [5]. Limestone aggregates experience less expansion than quartz and they maintain the same phase until their decomposition at 700 °C. However, cement paste expands slightly until 200 °C but, beyond these thresholds, starts to shrink rapidly due to the loss of combined water. This difference in strain behaviour develops an aggressive microcracking stage, which damages the interfacial transition zone (ITZ) between the cement paste and aggregates, and can even completely disconnect the aggregate from the paste. It is evident that the general behaviour of a structural element will be conditioned to the design of the concrete and its boundary conditions. In particular, water/binder ratio, moisture, type of aggregates, cement type and fiber inclusion are the most influencing variables in concrete's durability against high temperatures [3,2].

Because of the multiple causes that can affect the integrity of concrete, scientific communities are focused in the development of Non-Destructive Testing (NDT) techniques due to its robustness and its noninvasive nature. NDT can help to determinate the internal state of concrete structures *in-situ* or from extracted cores from pillars, walls or beams (among others). These techniques are classified according to the method for measuring the target scope of the structure. Beginning from mechanical waves, there are techniques for the purpose of overall inspection (e.g. ultrasonic and impact echo) and techniques for the purpose of surface evaluation (e.g. Schmidt rebound hammer, Windsor probe, and spectral analysis of surface acoustic waves) [6] . Other techniques focus on the response of specific points by obtaining concrete samples from different locations (e.g. small-scale mechanical testing, differential thermal analysis, thermogravimetric analysis, scanning electron microscopy or thermoluminescence analysis among others). Although some of these techniques are appropriate for *in-situ* test, it is hard to use them (e.g. Schmidt rebound hammer, Windsor prove, or impact echo) to characterise mesoscopic defects in global damage case. Others can sensitively evaluate contact-type defects but involve either time-consuming processes or limited potential for laboratory experiments due to their location (e.g. differential thermal analysis, thermogravimetric analysis, scanning electron microscopy).

Nonlinear Elastic Waves Spectroscopy (NEWS) [7] techniques such as Nonlinear Resonant Ultrasound Spectroscopy (NRUS) [8] or Nonlinear Impact Resonance Acoustic Spectroscopy (NIRAS) [9] can evaluate nonlinearity and hysteresis by analysing the relationship between the amplitude of excitation and the frequency response of a granular material. They offer interesting information about the mesoscopic defects in complex global damage cases such as thermal damage, where a different degradation mechanisms take place at the same time (e.g. stiffness loss and incompatibility of deformations etc.) with accessible and commonly available equipment [10,11]. Besides resonant techniques, ultrasonic attenuation and pulse velocity measurements can also be performed in the field with a relatively

simplicity and they can give interesting and specific information about the stiffness of the material and the scattering components. These variables become essential to evaluate the thermal damage of concrete, giving information about multiple processes inside the concrete elements [12,13,14,15,16] .

Several studies have analysed the case of thermal damage in concrete with NEWS techniques. Such studies monitor different temperatures of exposition to different concrete dosages, evaluating nonlinear acoustic parameters by means of NIRAS [17] and NRUS [18,19,20,21]. These studies also perform different tests to support the nonlinear acoustic results doing apparent expansion determinations [21] , semi-quantitative analysis on paste-aggregate images [18] and ultrasonic pulse velocity measurements [19,21] . The consideration of performing these additional tests lays on correlating them with the nonlinear parameters in order to determine the spoiling process of concrete, but analysing the loss of stiffness of the cement matrix and the aggregate debonding mechanism as a joint degradation phenomena in thermal damage of concrete.

The present study not only tries to correlate traditional parameters with NDT results on normalized mortar specimens at different temperatures, but also introduces a detailed analysis of the calculated parameters describing separately the loss of stiffness of the cement paste and the debonding mechanism of the aggregates. In addition, the effectiveness of the ultrasonic attenuation with a broadband chirp signal is discussed. The demonstration of the suitability of NIRAS and broadband frequency ultrasonic analysis as non-invasive techniques will help us to accurately analyse thermal damage in heterogeneous materials without compromising their integrity.

The paper is organized as follows: In section 1, we describe thermal damage in concrete, the NDT techniques that we have used and the scope of the paper. A description of the materials, layout and the explanation of the techniques are addressed in section 2. The results and correlation between the exposed techniques are found in section 3. Finally, the conclusions of the study are presented in section 4.

## 2 Experimental

### 2.1 Materials and specimens

Six mixes of standardised (UNE EN 196-1:2005) Portland cement mortar (water/cement = 0.5) made of 450 g of Spanish cement CEM I-52.5-R, 1350 g of 0/2 mm crushed quartz sand and 225 g of water were carried out to obtain 18 40×40×160 $mm^3$ specimens to perform the present study. Each mix of three specimens was used to reach the different temperatures of thermal damage. After the mixing process, iron moulds were stored in the wet chamber (20 °C and 100 % H.R.) for 24 hours. The mortar pieces were then released and stored in the wet chamber again for 60 days to reach the elastic properties stabilisation stage. the specimens were then dried to constant mass at 40 °C for 7 days and wrapped with plastic film until they reached room temperature again, which allowed us to characterise them in their pristine state. The thermal damage protocol was designed according to mass loss due to the decomposition of bonded water. A previous thermogravimetric (TG) analysis was undertaken to fix the analysis temperatures.

Figure 1 shows the derivative TG curve for a 0.5 w/c cement paste previously pulverised and treated with acetone and dried at 60 °C for 15 minutes. Analysed temperatures were established according to the beginning and ending of principal mass loss from the hydration products in the thermogram; thus, 90 ,150, 250, 400, 525 °C were selected.

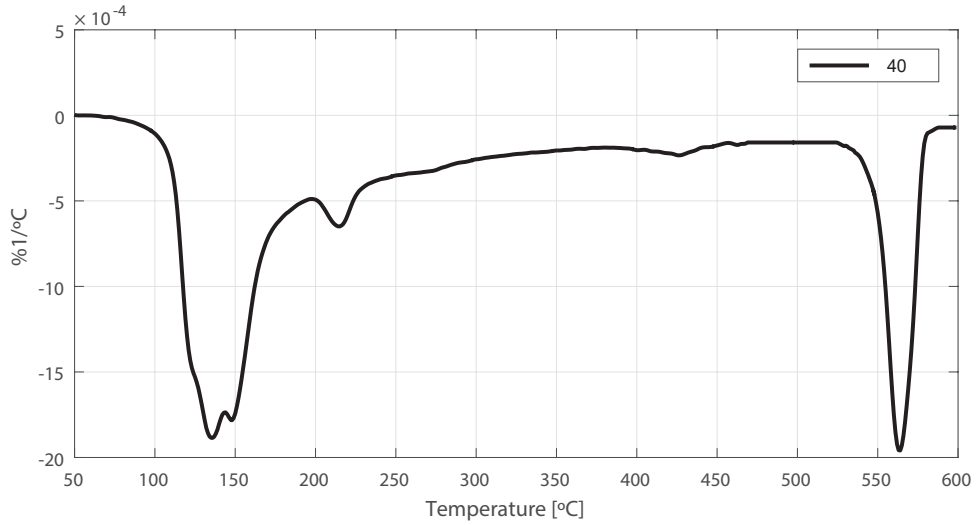


**Fig. 1:** DTG curve of a cured of 0.5 water to cement paste used select the analysed temperatures.

The analysis stopped in 525 °C due the phase change in silica sand to $\beta$-phase that brings the aggressive expansion of quartz. A programmable oven was used to damage the mortar bars. We increased the temperature at 3 °C /min rate until the desired temperature was reached. The temperature was then maintained for 3 hours. The oven was then switched off and cooled slowly for 24 hours.

## 2.2 Microstructural tests

These analyses were carried out on pastes, which had the same dosage as the mortars, excluding the sand. The thermogravimetry tests were performed to support the chemical decomposition of hydrated products for all analyzed temperatures. To carry out this analysis, portions of the paste samples were taken and pulverised with an agate mortar, adding a small amount of acetone. The solid was then filtered and dried at 60°C for 15 min. The equipment used was an ultrabalance Mettler TGA 850. Sealed aluminium crucibles of 100 ml were used, each with a micro-holed lid to create a water vapour self-generated atmosphere [22]. The analysis was carried out in a dry nitrogen atmosphere with a gas flow of 75 mL/min and a temperature interval of 35°C–600°C. For conventional thermogravimetric analysis, a 10°C/min heating rate was selected. The main decomposition DTG peak related to the calcium silicate hydrates is recorded in 110°C–130°C, that for the ettringite within the 140°C–150°C range, and those for the calcium aluminosilicate and calcium aluminate hydrates within the 210°C–220°C range [23]. Portlandite decomposition occurs between 500°C–600°C for the selected experimental conditions.

For the FESEM observations, portions of the paste and mortar subjected to 40 °C and 525 °C samples were taken, they were dried at 60°C and coated with a carbon layer. A ZEISS (ULTRA 55) electron microscope was used, set to voltage of 2–3 kV and to working distance between 3.9 mm and 6.0 mm.

## 2.3 Mechanical tests

Mechanical tests were performed to monitor the thermal damage process and correlate the destructive and conventional parameters with the nondestructive parameters. For the mechanical tests (determining the compressive and

flexural strengths), a universal testing machine was used (INSTRON model 3382) following the Spanish standard UNE-EN-196. For each analyzed temperature, three specimens were tested by means of three-point bending tests, and the six obtained semi-prisms were used to determine the compressive strength.

## 2.4 Dilatometry tests

A test to obtain the linear deformation of the pastes and mortar were performed. The equipment used for this experiment was an absolute dilatometer NETZSCH model 402-C, which was calibrated with a sapphire pattern. Special samples of mortar and paste of 10×10×60 $mm^3$ were used for this test. After the curing process, the samples were polished to the appropriate geometry for the dilatometer equipment (5×5×30 $mm^3$) and then dried during four days at 45 °. The thermal increment rate was 5 °C /min

## 2.5 Nondestructive test measurements

### *2.5.1 Nonlinear spectroscopy*

The NIRAS method is a relatively new NDT technique that can detect changes in materials from the resonance frequency shifts of the vibrational modes of a specimen as the impact energy increases. This change is simply due to the nonlinearity of the material. This technique has been shown to be highly high sensitivity to material defects, specifically to the microcracks of the material [9,10]. It is well-known that defects in a material can be detected from the vibrational frequency resonance values of a specimen made of that material. Distributed cracks reduce the stiffness of the specimen and, therefore, the natural frequency of the structural element made of that material. Besides this linear effect, cracks also change the nonlinear properties of the material making an imperfect matrix and nonhomogeneity zones that increment some mesoscopic effects. These kinds of imperfection trigger nonlinear effects, such as change of the frequency when the impact energy is increased, nonlinear modulation of two waves and scalability loss. This distortion of the elastic waves is responsible for the change in the observed resonance frequency in NIRAS tests, which can be described as a nonlinear hysteretic macroscopic behaviour of the material itself.

Two parameters were obtained with this layout. The dynamic moduli ($E_{dyn}$) were calculated following the expressions in the ASTM C215-14 with the linear frequency, and the nonlinear parameter $\alpha$ was related to frequency shift with the increase of the amplitude excitation. To calculate the nonlinearity of a single specimen, 10 impacts in an increasing amplitude were applied. From each vibrational signal, fundamental frequency, $f_i$ and its resonant amplitude, $A_i$ were extracted (figure 2a). The linear frequency, $f_0$, is obtained from the intersection with the y-axis at a virtual zero amplitude of a linear regression on a $A_i$ vs. $f_i$ plot of the 10 impacts [10]. Once the $f_0$ is determined, frequencies for each impact were normalised by the linear frequency and the linear regression of the normalised frequency vs. amplitude is recomputed to obtain the slope as $\alpha$ value (Eq. 1).

$$\frac{f_0 - f_i}{f_0} = \alpha \cdot A_i \tag{1}$$

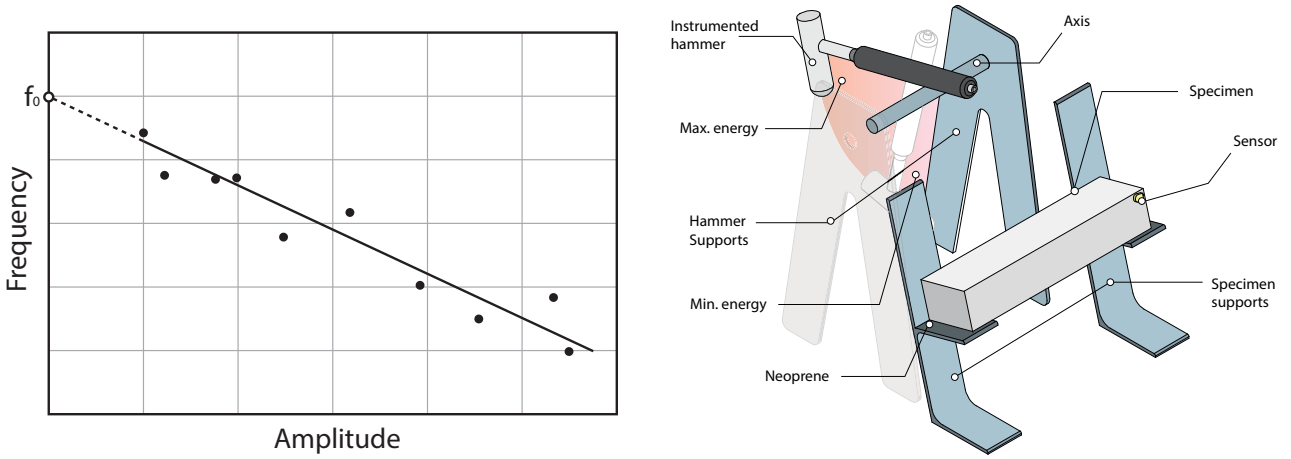


**Fig. 2:** Graphic information about vibrational setup and nonlinear parameter calculation. Figure 2a Amplitude vs. Frequency scheme for $\alpha$ calculation. Figure 2b Vibrational layout.

Acoustic resonance tests were performed with the setup presented in figure 2b. An impact hammer (Brüel & Kjær 8206-003) was attached to an axis, located in a metallic structure. This axis, supported on two ball bearings, yields a free rotational motion in one plane with minimum friction. The specimen was located in the metallic supports, slightly sloping, positioned for impact in the center of the face and perpendicular to the axis of greater inertia of its cross section. In the opposite top left-hand corner, a piezoelectric accelerometer sensor (PCB 352A21, 0.956 mV/m/s$^2$ sensitivity) was attached to obtain the vibrational motion of the test probe. The electric signal of the instrumented hammer and the accelerometer go through a signal conditioner (PCB 482A18) polarising it and transmitting it to the oscilloscope (Tektronics MDO3014). The oscilloscope was configured to optimise the signal acquisition and processing with $f_s$ equals to 250 kHz, N equals 10000 samples (40 ms acquisition time), trigger voltage equals to 120 mV and pre trigger time equals to 4 ms. Finally, the information was transmitted via USB to a computer with control software that was developed by the authors.

### *2.5.2 Ultrasonics*

Ultrasonic techniques have been widely used for materials characterisation and defect detection. A detailed analysis of the velocity and attenuation of the injected wave has been carried out in this study by means of broadband signals. Velocity is a well studied ultrasonic parameter that is directly related with the stiffness of the material. However, the attenuation phenomenon is closely related to the scattering media, being proportional to the injected frequency and the quantity and size of the elements of the specimen that may cause reflection, absorption and dissipation of the energy of the wave travelling through the media. The development of defects during a damage process in the material, such as debonding elements, micro-cracks or voids, will noticeably distort the geometry of the wave, and consequently, its energy.

In figure 3, the transmitted swept-frequency signal (chirp) $s_{tx}(t)$ can be observed. The mathematical expression of a linear chirp signal is shown in Eq. 2,

$$s_{tx}(t) = A_{tx} \sin\left(2\pi f_{min} t + \pi \Delta f_{max} t^2\right) \cdot rect\left(\frac{t - \frac{T}{2}}{T}\right) \tag{2}$$

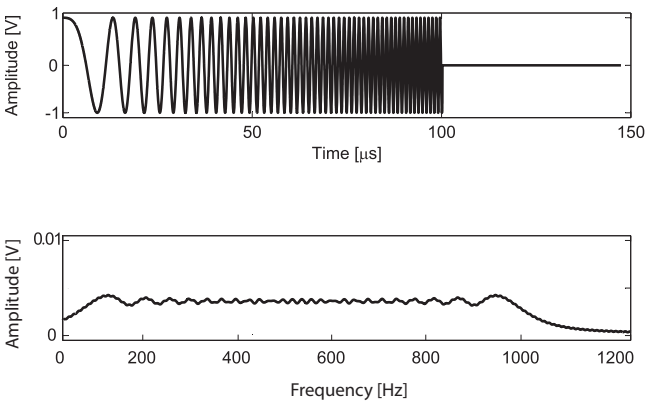


**Fig. 3:** Emitted signal in time and frequency domain.

$$\Delta f_{max} = \frac{f_{max} - f_{min}}{T} \tag{3}$$

where $A_{tx}$ is the amplitude of the signal, $t$ is the time, $f_{min}$ is the fundamental frequency, $T$ is the active time of the signal, and $\Delta f_{max}$ controls the maximum frequency ($f_{max} = f_0 + T\Delta f_{max}$) which is reached at $T$ seconds (Eq. 3). For this work and for the selected parameters are $A_{tx} = 1$ V, $f_0 = 100$ kHz, $f_{max} = 1$ MHz and $T = 100\mu s$.

The estimated ultrasound parameters are the wave velocity and the total attenuation of the material. The propagation velocity (or UPV), $v_p$, is obtained as the ratio between the length of the specimen, $d_{mat}$, and the signal time arrival, $t_a$ (Eq. (4)). The signal time arrival, $t_a$, was taken when the level of received signal exceeded 50% of the noise level.

$$v_p[m/s] = \frac{d_{mat}}{t_a} \tag{4}$$

The ultrasonic wave attenuation due to the material, $\alpha_{mat}(f)$, is calculated as the difference between the transmitted and received energies, taking into consideration the effect of the equipment and the distance travelled (Eq. 5).

The mathematical expression of the spectrum of the transmitted chirp signal attends to Eq. 6, and allows us to estimate $\alpha_{mat}(f)$ by applying Eq. 5 directly.

$$\alpha_{mat}(f) = \frac{10 \cdot log\left(S_{tx}(f)\right) - 10 \cdot log\left(S_{rx}(f)\right) - \alpha_{equip}(f)}{d_{mat}} \tag{5}$$

$$\begin{aligned} S_{tx}(f) = \Bigg| \frac{A_{tx}}{\sqrt{2\Delta_{f_{max}}}} e^{-j\pi(f-f_0)^2} \Bigg[ C\left(\sqrt{2}\frac{f-f_0}{\sqrt{\Delta_{f_{max}}}}\right) + jS\left(\sqrt{2}\frac{f-f_0}{\sqrt{\Delta_{f_{max}}}}\right) \\ - C\left(\sqrt{2}\frac{\Delta_{f_{max}}T + f - f_0}{\sqrt{\Delta_{f_{max}}}}\right) - jS\left(\sqrt{2}\frac{\Delta_{f_{max}}T + f - f_0}{\sqrt{\Delta_{f_{max}}}}\right) \Bigg] \Bigg|^2 \end{aligned} \tag{6}$$

where $C(x)$ and $S(x)$ are the Fresnel integrals. The received energy spectral density is computed as Eq. 7, where $X(f)$ (Eq. 8) is the Fourier Transform of signal $s_{rx}(t)$. As shown in Fig. 3, the spectrum of the transmitted pulse is

distributed along a frequency bandwidth. At the expense of decreasing the Signal to Noise Ratio (SNR), broadband signals excite several frequencies with a single signal. A single acquisition then allows us to compute the $\alpha_{mat}(f)$ curve from the theoretical transmitted and received spectra.

$$S_{rx}(f) = |X(f)|^2 \tag{7}$$

$$X(f) = \int_{t_0}^{t_1} x(t) e^{-i2\pi f t} dt \tag{8}$$

The attenuation associated with the measurement equipment (transducers, amplifier, wires, acquisition module, ... ), $\alpha_{equip}(f)$ [dB], is independent of the tested material and is constant over the test. The calibration process of the system was assessed with the same configuration but without the specimen under study because the transducers' surfaces face each other. For further details about the calibration process, see [13].

In this study, a through-transmission setup was selected because it offers good penetration and good accuracy to estimate the velocity and attenuation [24, 25]. Figure 4 shows the ultrasonic setup for this experiment. The transducers (transmitter and receiver) used were the K05SC from General Electric, which are both broadband transducers with a bandwidth centred at 0.5 MHz. The transmitter transducer was excited directly by a programmable signal generator (Handyscope HS3) and the reception transducer was connected to a 40 dB preamplifier (Panametrics 5600B).

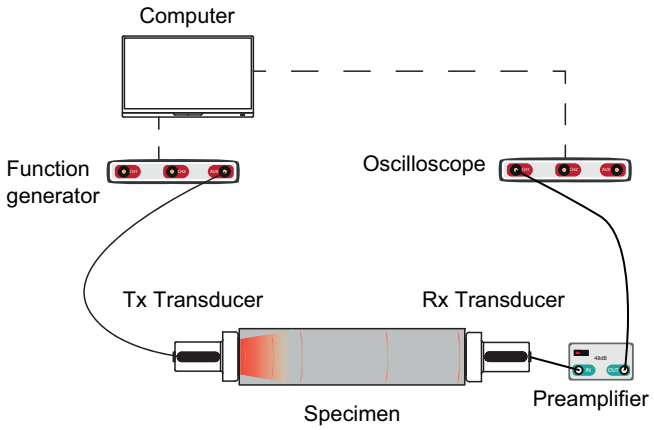


**Fig. 4:** Ultrasonic layout.

The received and amplified ultrasonic signal were captured by a digital oscilloscope (Handyscope HS3) with a sampling frequency of 50 MHz. HS3 is a double device that can be used simultaneously for both purposes; that is, signal generator and oscilloscope. Finally, a laptop was used to control the signal generator and to acquire and store the digitised signals. The ultrasonic transducers were placed facing the longitudinal axis of the prismatic specimen and they were fixed by a clamp. Petroleum jelly at the transducer–specimen interfaces was used as an impedance coupling medium.

## 3 Results

### 3.1 Microstructural tests

#### *3.1.1 Thermogravimetry*

The decomposition of different hydration products of Portland cement paste can be observed in thermogravimetry analysis. The derivative of mass loss curve for Portland cement pastes damaged at different temperatures is shown in figure 5. The typical decomposition peaks of this kind of material for all analyzed temperatures are shown.

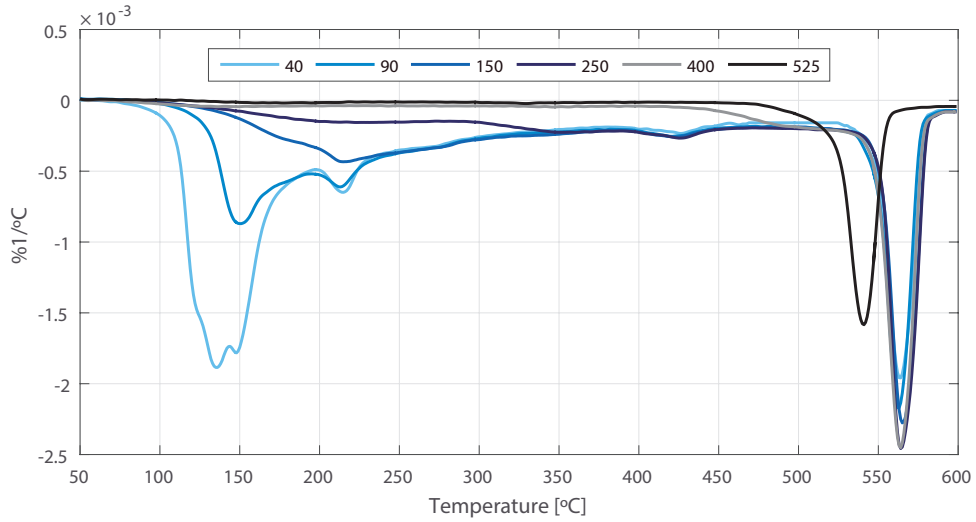


**Fig. 5:** DTG curves for all analysed temperatures [°C]

For the paste treated at 90 °C, a premature decomposition for C-S-H can be noticed respect to 40 °C series. This behaviour is attributed to the weakly bonded water in C-H-S gel, which is evaporated in the 40-90 °C range. For the paste treated at 150 °C, C-S-H and ettringite peaks almost completely disappeared. For pastes treated at 250 °C and 400 °C, no important changes happened in terms of thermal decomposition. At 525 °C, a displacement and decrement of the Portlandite peak occurs—this behaviour was attributed to the fact that part of the Portlandite was decomposed.

Table 1 shows the percentages of mass loss (relatives to the anhydrous mass) of the total water, Portlandite and hydrates for all of the tested temperatures. As the temperature increases, the total mass loss decreases due to the previous thermal treatment. Water associated to Portlandite remains constant or slightly increased due to the free Portlandite generated from the S-C-H and C-A-H decomposition for temperatures under 400 °C. However, water loss associated to Portlandite experiments huge decreases when 525 °C is reached due to its partial decomposition. The percentage of $H_2O$ loss respect to the water content for sample treated at 40 °C showed a continuous increase, reaching 81.07 % for 525 °C treatment. Evaporable (E) to non-evaporable (NE) material ratio is defined as the proportion of the combined water loss during the thermogravimetric test respect to the non-evaporable material, and it was calculated as (Combined $H_2O$)/(100-Combined $H_2O$).

**Table 1:** TG results based on anhydrous mass

| Temperature [°C] | Combined $H_2O$ [%] | E/NE ** | $H_2O$ from $Ca(OH)_2$ [%] | Portlandite [%] | $H_2O$ lost [%]* |
|---|---|---|---|---|---|
| 40 | 30.01 | 0.43 | 4.76 | 19.56 | 0.00 |
| 90 | 22.22 | 0.29 | 4.68 | 19.24 | 21.23 |
| 150 | 17.97 | 0.22 | 4.75 | 19.54 | 34.01 |
| 250 | 14.32 | 0.17 | 5.05 | 20.77 | 45.71 |
| 400 | 8.81 | 0.10 | 6.10 | 25.10 | 64.90 |
| 525 | 4.57 | 0.05 | 3.66 | 15.05 | 81.07 |

* Respect to 40 °C sample

** Evaporable (E) to non-evaporable (NE) material ratio (Combined Water/100-Combined Water)

### *3.1.2 Scanning Electron Microscopy*

Microscopy images were acquired with the aim of analyse differences between pristine and damaged samples in a micro and nanoscopic scales. To see the differences in the Portland cement matrix, pastes with 0.5 water to cement ratio were prepared and cured 90 days before exposing them to 40 and 525 °C. Figures 6a, 6b and 6c show pristine paste samples under SEM. In figure 6a, gel particles can be observed. These types of hydration products are the most common components in the Portland cement matrices. Ettringite needles and Portlandite formation can be distinguished in figures 6b and 6c surrounded by C-S-H. At the same magnifications, figures 6d, 6e and 6f show paste specimens exposed to 525 °C. In this series, mainly decomposition products from C-S-H and C-A-H products can be observed. Ettringite and Portlandite, which are noticeable in 40 °C treated samples, completely disappeared; as shown in the thermogravimetic analysis. Apparently, the morphology of the attacked C-S-H and C-A-H products cannot be easily distinguished from the pristine ones with a naked eye in SEM. A higher porosity in the microstructure (qualitatively, at the same magnification, more space between amorphous particles) of 525 °C sample may be noted, probably because a volume reduction generated in the bonded water loss from C-S-H.

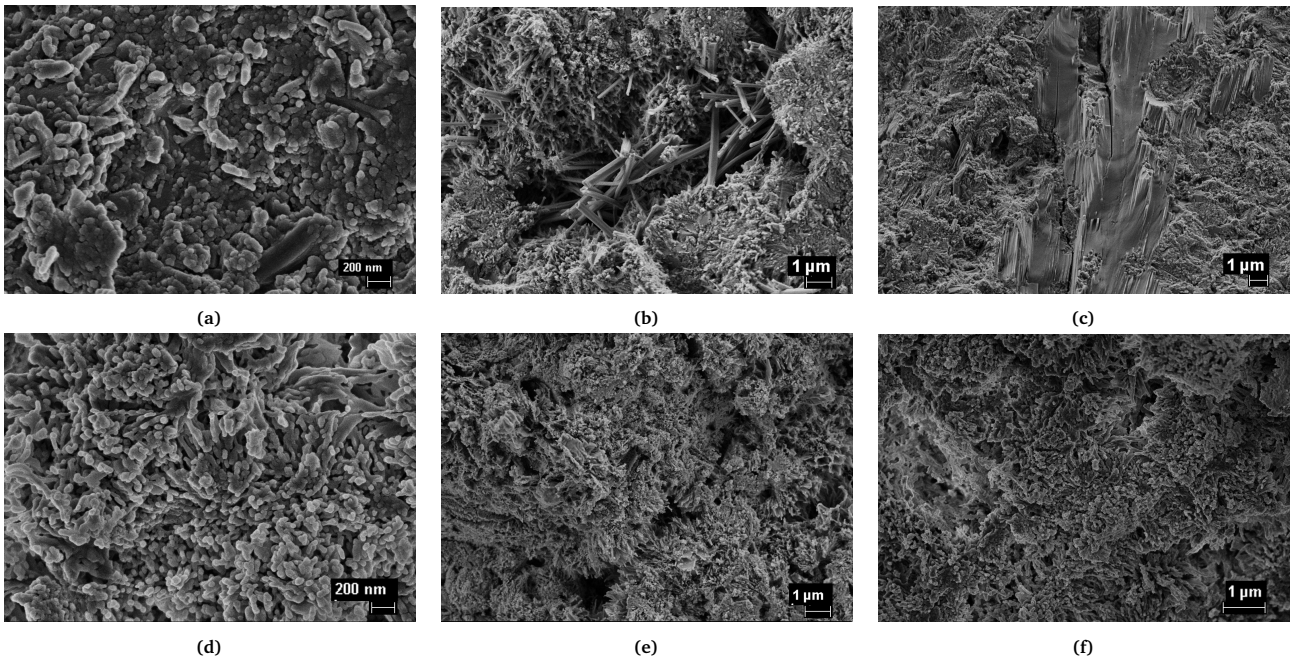


**Fig. 6:** FESEM micrographs of Portland cement pastes. Figs 6a,6b and 6c treated at 40 °C. Figs 6d,6e and 6f treated at 525 °C.

Figures 7a and 7b show optical microscopy images for polished sections of pristine (40 °C) and thermal damaged (525 °C) mortar samples. In figure 7a (40 °C), a highly cohesive material can be observed with strong matrix perfectly embracing the aggregates inside observed in optic microscope. In contrast, figure 7b (525 °C) shows remarkable fractures in the matrix in a radial direction surrounding the aggregates. The disconnection between cement paste and the aggregate becomes noticeable to the naked eye. Figures 7c and 7d show the SEM images for polished sections of pristine (40 °C) and thermal damaged (525 °C) mortar samples. It can be noticed that the roughness in thermal treated sample was significant, especially around the aggregate particles.

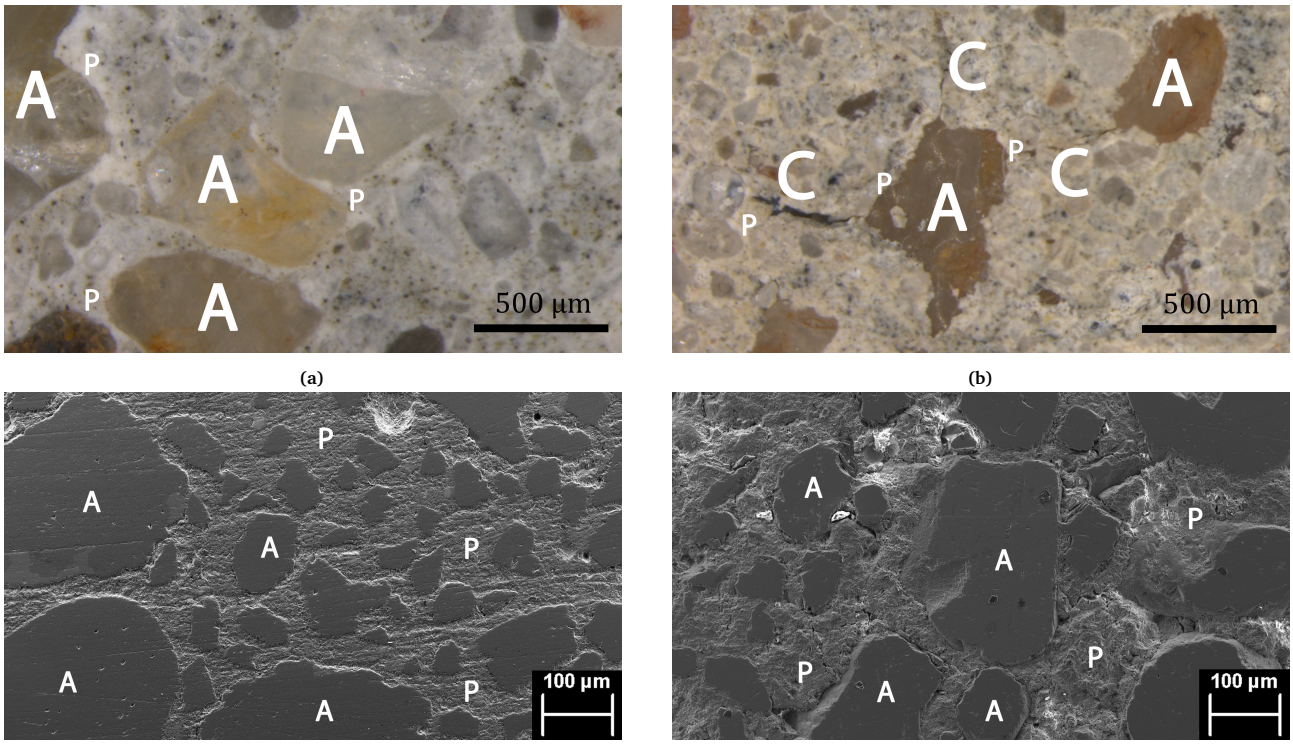


**Fig. 7:** Microscopy and optical images of polished mortar sections. Figure 7a shows an image of a pristine sample of mortar under optic microscope. Figure 7b shows an image of a thermal damaged (525 °C) sample of mortar under optic microscope. Figure 7c shows an image of a pristine sample of mortar under SEM. Figure 7d shows an image of a thermal damaged (525 °C) sample of mortar under SEM. Key: C= Crack, P= Paste, A= Aggregate.

Other authors did similar analysis evaluating the ITZ with microscope images for different temperatures. In the case of [18] researchers performed a semi-quantitative analysis in order to detect anomalies between aggregates and paste. In [21], authors did a complete image analysis on concrete samples in a qualitative way, supporting mechanical and NDT results in their study.

### 3.2 Physical and mechanical tests on mortar

Several different kinds of physical tests were performed to distinguish the different mechanisms of degradation in the thermal damage on cementitious materials. Three additional specimens per analyzed temperature were manufactured due to the destructive nature of the compression and flexural strength tests. Figure 8a shows the mass loss due to the debonded water in the hydration products of Portland cement. As can be observed, the mass of specimens decreases in a nonlinear trend as the temperature increases. Nonetheless, the mechanical performance of the elements increases during this heat thermal treatment, as shown in figures 8b and 8c until 150° C. This slight improvement (or conservation) in the strength could be attributed to an increase in curing speed rate of the element mortar during heating, directly enhancing its mechanical properties. After 150° C, mechanical strength starts a decay process during the rest of the thermal tests, especially for 400 ° C and 525 ° C.

To understand the degradation process, figure 8d should be analyzed in detail. In this figure, relative longitudinal elongation (strain) was plotted for paste ($S_p$) and mortar ($S_m$) samples. These specimens were made with the equivalent dosage presented in the previous section. In the first instance, from 20 ° C to 150 ° C paste and aggregate expands at the same rate, being paste and mortar series quasi-coincident. After this temperature, a differentiation in behaviour between mortar and paste occurs due to a trend change until 350 ° C. Beyond 350 ° C, the negative slope of deformation increases for paste while mortar continues expand linearly. This test reveals the incompatibility of thermal deformations between the paste and aggregate, giving clear evidence for the damage produced by the increment of the temperature. This is a complex mechanism that not only involves the destruction of hydrated products of the cement paste but also includes the difference in thermal strain of the raw constituent materials that are part of the mortar sample. In order to quantify the debonding process and ITZ spoil, authors have considered the use of this technique due to the precision on the monitoring of the different strain behaviour developed by the components of mortar submitted to high temperatures. In Section 3.4 this behaviour is analysed in detail as the relative difference between paste and mortar strain in absolute value ($|S_m\text{-}S_p|$).

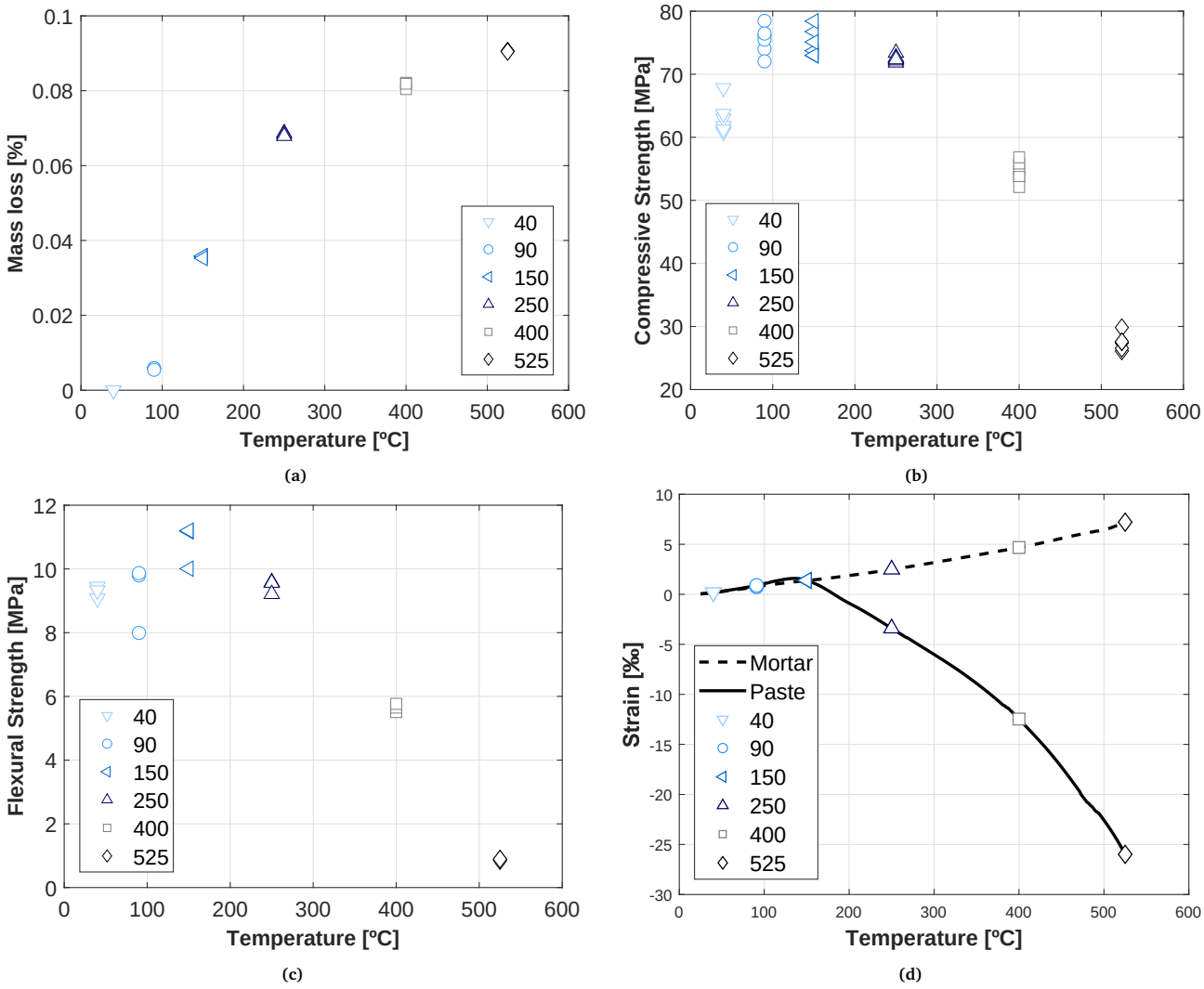


**Fig. 8:** Physical and mechanical tests performed to the material for all monitored temperatures. Figure 8a shows mass loss. Figure 8b shows compressive strength. Figure 8c shows flexural strength. Figure 8d shows dilatometry.

## 3.3 Nondestructive technique measurements

### *3.3.1 Nonlinear spectroscopy*

The Nonlinear Impact Resonance Acoustic Spectroscopy (NIRAS) technique can extract nonlinear elastic and hysteresis information of mesoscopic materials such as mortar or concrete. Figure 9a represents the elastic modulus extracted from linear frequency ($f_0$) from the NIRAS test. The plot clearly defines a decay of the stiffness on mortar elements due to mass loss that is directly related to debonding water of the hydrated Portland cement matrix. Furthermore, two different linear trends can be identified: from 40 to 250 °C (lower slope) and 250 °C to 525 °C (higher slope). In following sections these trends are correlated to microstructural parameters. These results are in agreement with the literature taking into account the differences in the nature of the aggregates [19].

Hysteretic parameter reveals important information about the internal state of the material. As can be observed, $\alpha$ values remains constant before 250 °C. After this temperature, $\alpha$ values increases to higher values during the experiment (an increase of 300 % from 250 to 400 series, and an increase of % 200 from 400 to 525 series). As observed in the previous section, in figure 8d, the huge differences between the deformation of the aggregate and the

paste, force the aggregate to separate from the paste. This phenomena increases the nonlinearity and hysteresis of the system, raising the number of contacts between particles and mesoscopic discontinuities. This process is the only one provoking a real decay in the global performance of the material because the mass loss only affects its softening. Studies on thermal thermal damage in concrete and mortar using nonlinear vibration techniques have shown similar results: in the case of NRUS techniques in [18,19], noticeable increasing on the nonlinear parameter is detected after 250 °C. However, noticeable differences can be found in other studies due to the different amount of aggregate respect to the paste content (1:5.76 cement to aggregate ratio) and its maximum size (19mm) [17]. In this case, the hysteretic parameter grows for every evaluated temperatures.

Apparently, linear and nonlinear parameters extracted by means of NIRAS test allows to characterize the different complex mechanisms of degradation that take place in the system at the same time. In following sections, these mechanisms and its relation with NIRAS parameters are analyzed in detail.

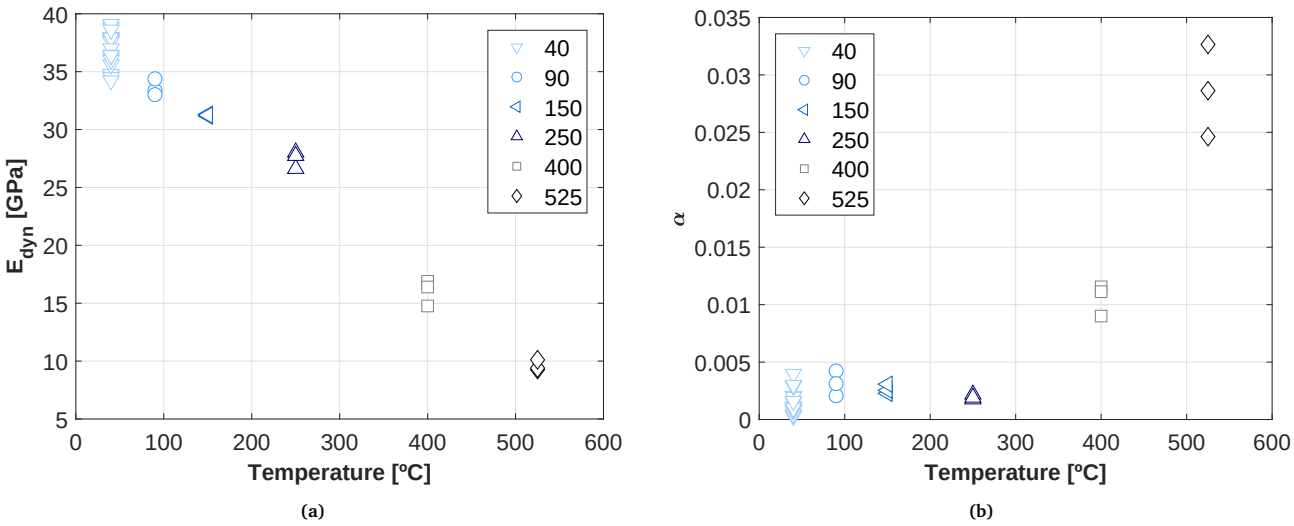


(a) (b)

**Fig. 9:** Vibrational test performed on the material for all monitored temperatures. Figure 9a shows the dynamic modulus. Figure 9b shows the hysteretic parameter.

### *3.3.2 Ultrasonics*

Ultrasonic tests reveal information about the changes in a mechanical wave travelling through a material, which is unlike vibration tests where the material resonates in its principal modes after an excitation. The pulse velocity and attenuation of wave energy are complementary parameters extracted from the ultrasonic signal. From this, it can be registered different kind of information from the material. Pulse velocity is more related to the stiffness of the material, being proportional to the dynamic modulus. However, attenuation is more related to the dispersive elements inside material, such as aggregates, voids and micro-cracks.

Figure 10a shows the changes in ultrasonic pulse velocity for all specimens. As can be observed, the nonlinear negative trend can be revealed as the temperature rises. This behavior matches with the trend of $E_{dyn}$ extracted from NIRAS test since velocity is squared in dynamic modulus equation when it is extracted from p-wave and s-wave velocity [6]. As commented in vibration tests, the stiffness on mortar elements decays due to mass loss, which is directly related to debonding water from the hydrated Portland cement matrix.

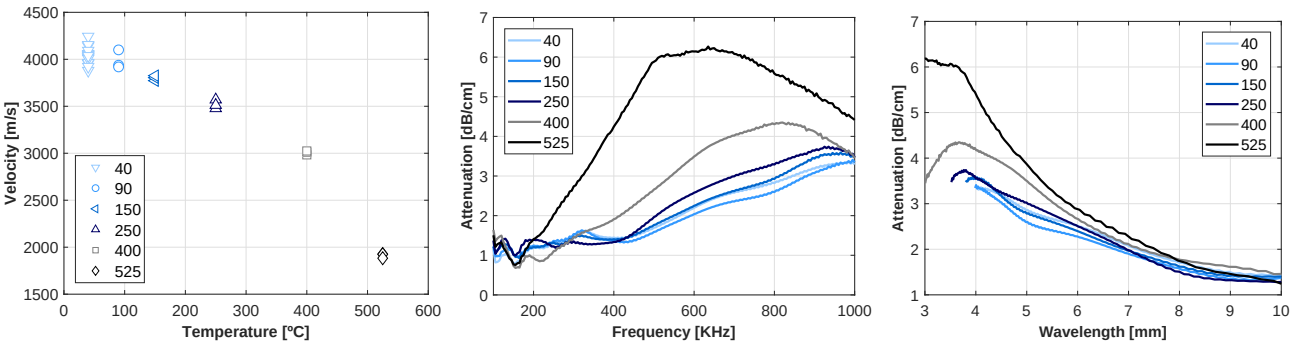


**Fig. 10:** Ultrasonic test performed to the material for all monitored temperatures. Figure 10a shows the ultrasonic pulse velocity. Figure 10b shows the attenuation. Figure 10c shows the attenuation curves versus wavelength calculated from velocity in figure 10a.

In figure 10b, attenuation versus frequency curves are plotted for different temperatures. Because frequency is inversely proportional to wavelength (Figure 10c), the increment of frequency in ultrasonic inspections implies that it is more sensitive to small defects and discontinuities. This means that the attenuation mechanism (absorption and reflection, mainly) reveals the global status of the material, being an interesting phenomena to analyze pores, cracks and defects. As can be observed, mortars submitted to thermal treatment at 40, 90 and 150 °C present almost the same attenuation values for all frequency ranges. From samples submitted in the 250 °C to 400 °C range, a huge change in attenuation values from 600 to 900 KHz was noted (an increase of 1 dB/cm). This behavior explains the paste-aggregate separation forced by the incompatibility of the deformation between them. For 525 °C series, a high attenuation behavior for all frequency range was noted, rising to higher values (2 dB/cm difference between 400 and 525 series) with a noticeable slope since 100 KHz provoked by the softening of the Portland cement matrix, induced micro cracking and the degradation of interfacial transition zone between the paste and the aggregate.

### 3.4 Parameters correlation

The presented results have shown the evolution of microstructural, physical and NDT parameters when different temperatures are applied to mortar samples. As described in the introduction, thermal damage in mortar and concrete has been widely studied from different perspectives and tests. As novelty, in this section the calculated parameters are correlated between them, pointing out the importance of the influence of the aggregates debonding mechanism and the loss of stiffness of the cement paste, the moment when they start their effects and the influence of the combination of both mechanism after a threshold temperature. Two different physical and microstructural parameters are proposed in order to quantitatively evaluate these two mechanisms of damage: the Evaporable to Non Evaporable material ratio (E/NE) as an indicator of the loss of the stiffness in the cement matrix, and the relative difference between paste and mortar strain in absolute value ($|S_m\text{-}S_p|$) as an indicator of aggregate debonding process. Figure 11 shows the variation of E/NE and $|S_m\text{-}S_p|$ for every analysed temperature. Up to 150 °C, there is no variation in the $|S_m\text{-}S_p|$ while E/NE is moving to lower values. From 250 °C, the two parameters change, combining the effects of the two aforementioned damage mechanisms.

In this section, E/NE and $|S_m\text{-}S_p|$ are correlated with all NDT parameters, establishing clear connections between them and testing their sensitivity. Figure 12a and 12c show the evolution of dynamic modulus and ultrasonic velocity

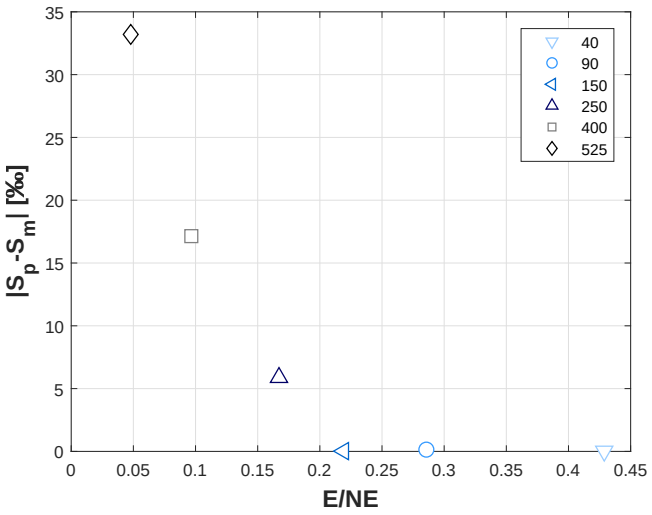


**Fig. 11:** Evaporable to Non Evaporable ratio (E/NE) and the relative difference between paste and mortar strain in absolute value ($|S_m\text{-}S_p|$) for the evaluated temperatures.

versus E/NE, respectively. Since $E_{dyn}$ and $v_p$ are proportional to the stiffness of the material, these parameters evolve with the same trend. In addition, a change in the trend can be noticed at 250 °C due to the combination of the two damage mechanisms: the material losses stiffness faster because the debonding process of the aggregates and the evaporation of hydrated compounds of the cement paste happens at the same time. However, when these parameters are plotted against $|S_m\text{-}S_p|$ (Figures 12b and 12d), no significant variation can be observed until 250 °C. After that, a noticeable linear decay of these parameters can be observed.

Figures 13a and 13c shows the evolution of nonlinear parameter $\alpha$ and ultrasonic attenuation at a fixed frequency (authors chosen 600 KHz because more differences can be noticed at this frequency) versus E/NE, respectively. These parameters seem to be more sensitive to cracks and voids and not to the loss of stiffness due to the change in the microstructure of the cement paste as described in the previous section. It is important to point out the slight difference at 250 °C between attenuation and $\alpha$: attenuation changes at this point while $\alpha$ do not rise to higher values until 400 °C. Figure 13c and 13d shows the evolution of these parameters versus $|S_m\text{-}S_p|$. In this graphs, no variations in the parameters can be noticed until 250 °C in the case of ultrasonic attenuation. A linear variation of $\alpha$ and attenuation can be seen for the rest of the analysed temperatures.

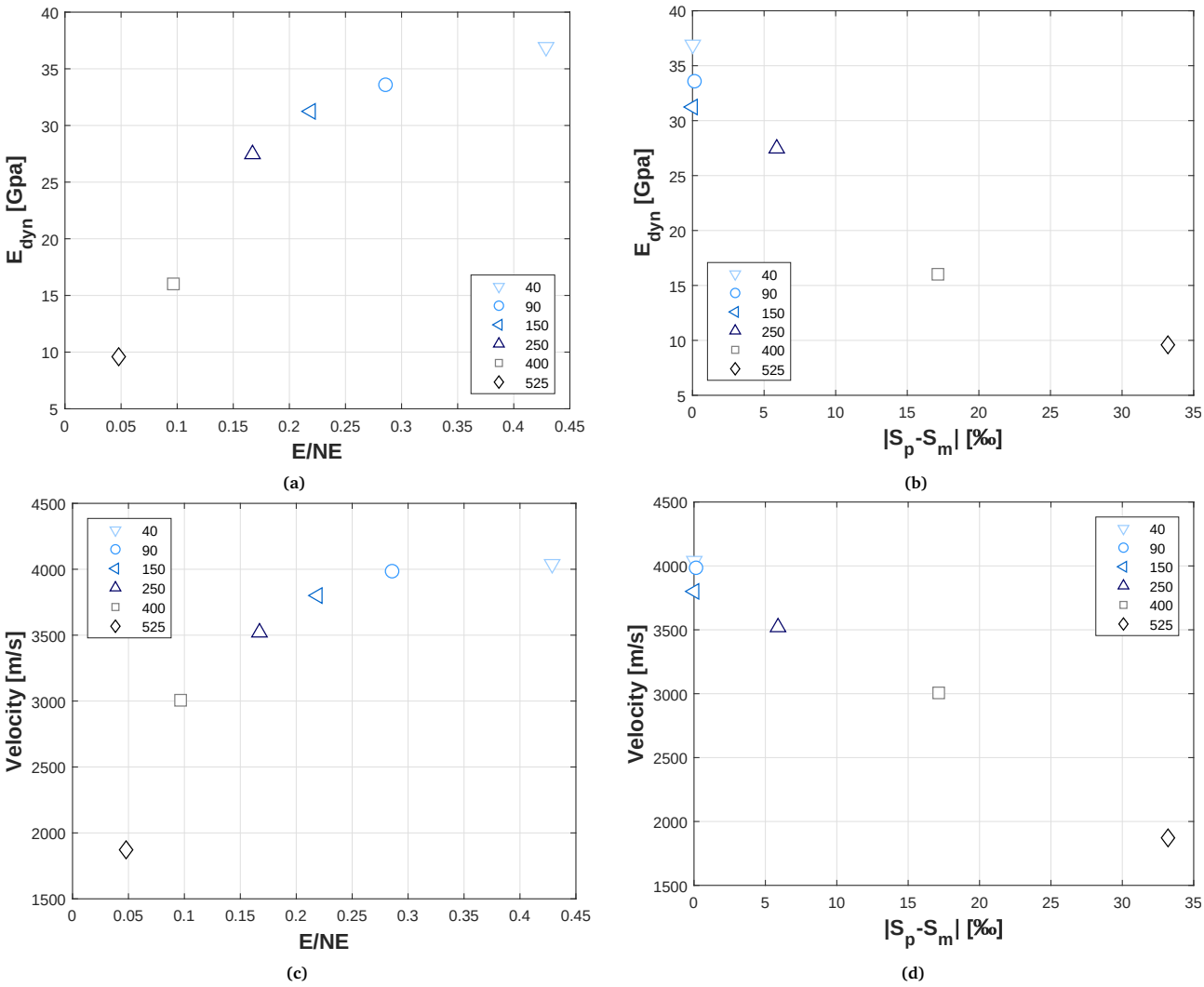


**Fig. 12:** Evaporable to Non Evaporable ratio (E/NE) and the relative difference between paste and mortar strain in absolute value ($|S_m\text{-}S_p|$) versus NDT parameters related to the stiffness loss of the paste ($E_{dyn}$ and velocity).

## 4 Conclusions

Thermal attack in concrete is a complex mechanism of damage. Temperature not only affects the cement matrix but also leads to the incompatibility of deformation between aggregate and paste. In this study a complete analysis of this kind of damage is addressed, not only with traditional methods but also by trying to capture the intricate system with nondestructive tests, and also analyse and correlate the obtained data with physical and microstructural tests for different temperatures between 40 °C and 525 °C.

Microstructural analysis (Thermogravimetry and Scanning Electron Microscopy) showed the principal changes of the Portland cement hydrated products for the different analysed temperatures. Compressive and flexural strength results remained constant or even increase at low temperatures (up to 250 °C), meanwhile the mass loss increases. The dilatometry results revealed important information about deformation incompatibilities between the paste and the aggregate. These results have been correlated with nondestructive tests: nonlinear impact resonance acoustic spectroscopy and ultrasonic measurements. The dynamic modulus and ultrasonic pulse velocity have closely measured the linear stiffness decay of the specimens. However, hysteretic parameter exhibited different trend from stiffness-related parameters, keeping constant until 250 °C and performing a huge change for 400 and 525 °C. Ultrasonic

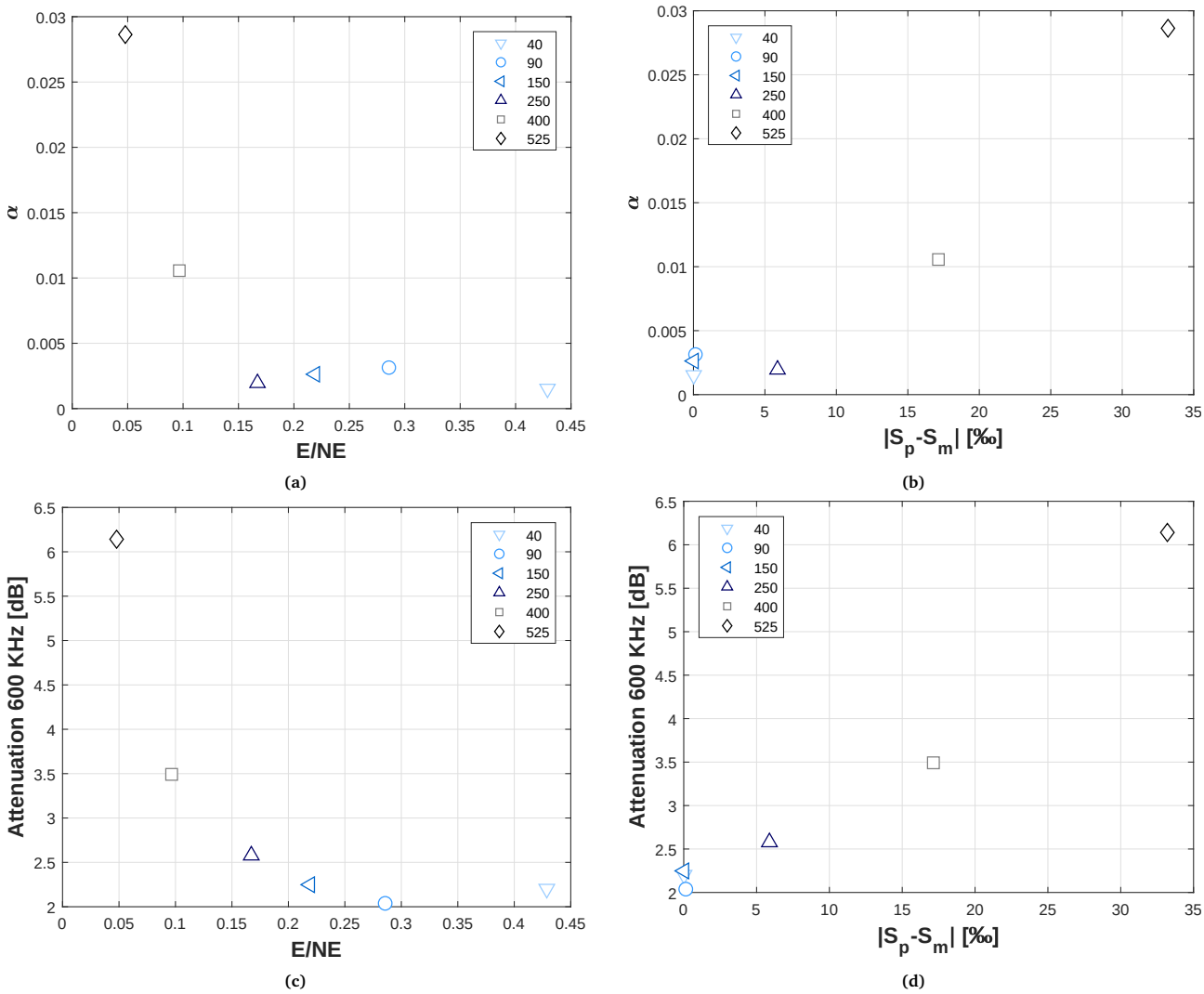


**Fig. 13:** Evaporable to Non Evaporable ratio (E/NE) and the relative difference between paste and mortar strain in absolute value ($|S_m\text{-}S_p|$) versus NDT parameters related to aggregate debonding mechanism ($\alpha$ and attenuation).

attenuation computed with a broadband ultrasonic signal (chirp) unveiled true information in one single signal about scattering components inside the material, being sensitive to interfacial transition zone between aggregate and paste in a large range of frequencies. The correlation between microstructural, mechanical and nondestructive techniques were carried out successfully, being nonlinear vibration and ultrasonic attenuation non-conventional parameters that gave crucial of information about a complex damage process, such as thermal attack in highly heterogeneous materials (e.g. Portland cement composites).

## Acknowledgements

This work has been supported by the Spanish Administration under grants, BES2015-071469, under the ONDATEST coordinated project, BIA2014-55311-C2-1-P and BIA2014-55311-C2-2-P. Thanks are given to FEDER funds for co-funding.

## References

1. P.C. Aïtcin, *Binders for durable and sustainable concrete* (2008)

2. Q. Ma, R. Guo, Z. Zhao, Z. Lin, K. He, Construction and Building Materials **93**, 371 (2015)
3. U. Schneider, Fire Safety Journal **13**(1), 55 (1988)
4. C.R. Cruz, M. Gilien, Fire and Materials **4**(2), 66 (1980)
5. A.H. Jay, Proceedings of the Royal Society of London. **142**(846), 237 (1933)
6. V. Malhotra, N. Carino, *Handbook on Nondestructive Testing of Concrete*. Civil engineering (CRC Press, 2004)
7. K. Van Den Abeele, J. Carmeliet, J.A. Ten Cate, P. Johnson, Research in Nondestructive Evaluation **12**(1), 17 (2000)
8. P.A. Johnson, A. Sutin, in *AIP Conference Proceedings* (2005)
9. K.J. Leśnicki, J.Y. Kim, K.E. Kurtis, L.J. Jacobs, NDT & E International **44**(8), 721 (2011)
10. S.J. Park, H.J. Yim, H.G. Kwak, Fire Safety Journal **69**, 36 (2014)
11. U. Dahlen, N. Ryden, A. Jakobsson, NDT and E International **75**, 15 (2015)
12. V. Genovés, A. Carrión, J. Gosálbez, I. Bosch, M.V. Borrachero, J.J. Payá, (1)
13. V. Genovés, J. Gosálbez, A. Carrión, R. Miralles, J. Payá, Ultrasonics **65**, 345 (2016)
14. T.P. Philippidis, D.G. Aggelis, Ultrasonics **43**(7), 584 (2005)
15. M. Molero, I. Segura, S. Aparicio, M.G. Hernández, M.a.G. Izquierdo, Ultrasonics **50**(8), 824 (2010)
16. V. Genovés, F. Vargas, J. Gosálbez, A. Carrión, M. Borrachero, J. Payá, Materials & Design **125**(Supplement C), 46 (2017)
17. G.K. Park, H.J. Yim, International Journal of Concrete Structures and Materials **11**(3), 447 (2017)
18. C. Payan, T. Ulrich, P. Le Bas, M. Griffa, P. Schuetz, M. Remillieux, T. Saleh, Applied Physics Letters **104**(14), 144102 (2014)
19. C. Payan, T.J. Ulrich, P.Y. Le Bas, T. Saleh, M. Guimaraes, The Journal of the Acoustical Society of America **136**(2), 537 (2014)
20. C. Payan, V. Garnier, J. Moysan, P. Johnson, The Journal of the Acoustical Society of America **121**(4), EL125 (2007)
21. H.J. Yim, J.H. Kim, S.J. Park, H.G. Kwak, Cement and Concrete Research **42**(11), 1438 (2012)
22. M.V. Borrachero, J. Payá, M. Bonilla, J. Monzó, Journal of Thermal Analysis and Calorimetry pp. 503–509 (2008)
23. V. Genovés, L. Soriano, M. Borrachero, J. Eiras, J. Payá, Construction and Building Materials **78**, 295 (2015)
24. J. Krautkrämer, H. Krautkrämer, *Ultrasonic testing of materials* (Springer-Verlag, 1983)
25. P.A. Gaydecki, F.M. Burdekin, W. Damaj, D.G. John, Measurement Science and Technology **3**(1), 126 (1992)